LIFE SCIENCES

Structure of the human Meckel-Gruber protein Meckelin

Dongliang Liu[1,2,3]†, Dandan Qian[4]†, Huaizong Shen[1,2,3], Deshun Gong[4]*

Mutations in the *Meckelin* gene account for most cases of the Meckel-Gruber syndrome, the most severe ciliopathy with a 100% mortality rate. Here, we report a 3.3-Å cryo–electron microscopy structure of human Meckelin (also known as TMEM67 and MKS3). The structure reveals a unique protein fold consisting of an unusual cysteine-rich domain that folds as an arch bridge stabilized by 11 pairs of disulfide bonds, a previously uncharacterized domain named β sheet–rich domain, a previously unidentified seven-transmembrane fold wherein TM4 to TM6 are broken near the cytoplasmic surface of the membrane, and a coiled-coil domain placed below the transmembrane domain. Meckelin forms a stable homodimer with an extensive dimer interface. Our structure establishes a framework for dissecting the function and disease mechanisms of Meckelin.

INTRODUCTION

Primary cilia are microtubule-based organelles that protrude apically from the surface of almost all polarized cell types of the human body (*1*). These hair-like structures have essential roles throughout development in mechanosensation (*2*, *3*) and signal transduction by the Hedgehog (Hh)–, Wnt-, and platelet-derived growth factor receptor alpha signaling pathways (*4*–*6*) and in the determination of left-right asymmetry (*7*). Defects of primary cilia have been associated with a broad spectrum of more than 35 human genetic diseases called ciliopathies (*8*). The transition zone (TZ), a compartment of the proximal region of cilia, acts as a diffusion barrier that controls the entry and exit of more than 700 ciliary proteins into cilia (*9*). A special module at the TZ known as MKS-JBTS (Meckel-Gruber syndrome–Joubert syndrome) is composed of many of the proteins mutated in MKS and JBTS (*10*–*12*).

MKS, also known as Meckel syndrome or Gruber syndrome, was first described by Johann Friedrich Meckel in 1822. In 1934, G. B. Gruber described the same condition and named it dysencephalia splanchnocystica (*13*). MKS is a rare lethal autosomal recessive condition with a neural tube defect leading to death of the fetus in utero or shortly after birth, representing the most severe ciliopathy with a 100% mortality rate (*13*). MKS is characterized by three classic symptoms—polycystic kidneys (observed with a frequency of 100%), occipital encephalocele (90%), and postaxial polydactyly (83.3%) (*14*)—and is accompanied by other abnormalities, including oral clefting, genital anomalies, central nervous system malformations, and liver fibrosis.

The worldwide incidence of MKS ranges from 1:13,250 to 1:140,000 live births, but higher incidences are observed in endogamous populations, such as the Gujarati Indians, who have a prevalence of 1 in 1300 (*15*, *16*). MKS has extreme genetic heterogeneity and displays allelism with other ciliopathies, such as JBTS, COACH (cerebellar vermis hypoplasia, oligophrenia, ataxia, coloboma, and hepatic fibrosis) syndrome, orofaciodigital syndrome, nephronophthisis, and Bardet-Biedl syndrome (*13*).

To date, mutations in 14 genes have been described as a cause of MKS (*13*). Notably, mutations in Meckelin account for 16% of MKS cases, representing the most frequent cause of MKS (*17*). Meckelin mutations are also a major cause of JBTS and COACH (*17*–*19*). JBTS is a rare brain malformation characterized by the absence or underdevelopment of the cerebellar vermis, an area of the brain that controls balance and coordination, and a malformed brain stem (molar tooth sign) (*20*). COACH is a condition that mainly affects the brain and liver (*21*).

Meckelin, a 995–amino acid transmembrane protein, contains a signal peptide, an extracellular N-terminal cysteine-rich domain (CRD), a predicted β sheet–rich region, seven predicted transmembrane regions, and a coiled-coil (CC) domain (*12*, *19*). Although Meckelin does not share substantial homology with the Frizzled (FZD) proteins, which are class-F G protein–coupled receptors (GPCRs) that have versatile roles in signal transduction during differentiation and development by acting as Wnt receptors (*22*), Meckelin is hypothesized to be a protein with topological similarity to this family because they all contain a CRD and a seven-transmembrane α-helical bundle structure (*19*, *23*). However, there is no evidence of Meckelin being a GPCR, and it remains to be seen whether there is structural similarity between Meckelin and class-F GPCRs.

Owing to the pathological importance of Meckelin, the physiological functions of Meckelin have been investigated in several studies. Meckelin localizes to the primary cilia, basal body, and plasma membrane (*24*, *25*). Meckelin is required for centrosome migration to the apical membrane and the consequent formation of primary cilia (*26*). In addition, Meckelin can interact with MKS1 and TMEM216, both of which are also mutated in MKS and required for centrosome migration during ciliogenesis (*25*, *26*). For ciliogenesis to occur, the cell must first display polarity, a process dependent on actin remodeling (*27*, *28*). Meckelin can interact with the actin-binding isoform of nesprin-2 (nuclear envelope spectrin repeat protein 2) (*29*), an important scaffold protein required in the maintenance of the actin cytoskeleton, and actin-binding protein filamin A (*25*), a key organizer of the actin cytoskeleton, mediating ciliogenesis (*25*, *29*). Recently, it has been suggested that Meckelin can function as a receptor of β-catenin–independent signaling that binds to Wnt5a and mediates downstream signaling through receptor tyrosine

[1]Key Laboratory of Structural Biology of Zhejiang Province, School of Life Sciences, Westlake University, Hangzhou, Zhejiang 310024, China. [2]Westlake Laboratory of Life Sciences and Biomedicine, Hangzhou, Zhejiang 310024, China. [3]Institute of Biology, Westlake Institute for Advanced Study, Hangzhou, Zhejiang 310024, China. [4]State Key Laboratory of Medicinal Chemical Biology and College of Life Sciences, Nankai University, Tianjin 300350, China.
*Corresponding author. Email: gongds@nannkai.edu.cn
†These authors contributed equally to this work as first authors.

kinase-like orphan receptor 2 as a coreceptor, thereby controlling basal body positioning and epithelial branching morphogenesis (*12*). In addition, Meckelin can also regulate Wnt/β-catenin–dependent signaling in the developing cerebellum via Hoxb5 (homeobox-type transcription factors) (*30*) and cause polycystic kidney disease through ERK1/2 (extracellular signal–regulated kinase 1/2)– and JNK (c-Jun N-terminal kinase)–dependent signaling pathways (*31*). However, the precise functional role of Meckelin remains enigmatic.

Despite some advances in understanding the functional aspects of Meckelin, the current lack of any structural information regarding Meckelin has hindered understanding of its mechanism of action and research into drugs that target it. Here, we report the structure of full-length human Meckelin protein at an overall resolution of 3.3 Å, determined using single-particle cryo–electron microscopy (cryo-EM).

RESULTS

Structural determination of Meckelin

The detailed protocols of the protein purification, sample preparation, cryo-EM data acquisition, and structural determination are presented in Materials and Methods, figs. S1 to S7, and table S1. The overall resolution of the EM map without imposing symmetry was calculated to be 3.4 Å of 219,967 selected particles according to the gold-standard Fourier shell correlation 0.143 criterion (figs. S2 and S3). Docking of the model of the protomer with better resolution into the low-pass–filtered EM map of the opposing protomer supports that the two CC domains have the same conformation (fig. S4A). The final resolution increased to 3.3 Å when C2 symmetry was applied (figs. S2 and S3).

The 3.3-Å EM map displays excellent main chain connectivity and side chain densities for almost all residues of Meckelin (fig. S5), except those of the CC domain, enabling us to build de novo atomic models for the N-terminal CRD, the β sheet–rich domain (hereafter BRD), and the transmembrane domain (TMD) (figs. S5 to S7). In addition to many bulky residues, such as Phe, Tyr, Trp, and Arg, there are four glycosylation sites and 12 disulfide bonds in the extracellular domain (ECD; containing CRD and BRD), in turn, validating the sequence assignment. The main chain of the CC domain can be reliably traced according to the EM map with symmetry expansion, wherein the side chain densities of some bulky residues in the CC domain are well resolved (figs. S4B and S5C).

Overall structure of Meckelin

The overall structure of Meckelin has dimensions of approximately 155 Å by 90 Å by 55 Å (Fig. 1 and fig. S1C). The structure reveals a dimeric assembly through an extensive dimer interface, including both the ECD and TMD (Fig. 1). The CRDs form a dimer with an antiparallel pattern. The N terminus of the CRD of one protomer reaches a pocket formed by the BRD of the opposing protomer (BRD′) (Fig. 1). In addition, the N-terminal half of the CRD of one protomer is extended into the vicinity of the C-terminal half of the CRD′, displaying a domain swap configuration (Fig. 1). BRDs interact with each other and serve as a linker between the CRD and TMD (Fig. 1). The two helices of the CC domain are placed below the TMD (Fig. 1).

The structure of CRD

CRDs, a landmark of the class-F GPCR family including Smoothened (SMO) and 10 FZD subtypes, have central roles in mediating Wnt and Hh signaling pathways by recognizing Wnt (for FZDs) and cholesterol molecules (for SMO) (*32*, *33*). Obviously, the Meckelin-CRD shows no similarity to the class-F GPCRs-CRDs (fig. S9). For structure, in contrast to the five pairs of disulfide bonds formed by 10 cysteines without a particular order of class-F GPCRs-CRDs, the Meckelin-CRD (residues 37 to 280) contains 11 pairs of disulfide bonds arranged in sequence (Fig. 2, A and B, and figs. S8A and S9). It resembles an arch bridge spanning approximately 60 Å with a height of approximately 35 Å, wherein the 11 pairs of disulfide bonds in each protomer maintain their stability and rigidity (fig. S8A). The CRDs of class-F GPCRs comprise four helices with three ligand-binding sites (fig. S10A) (*34*, *35*), whereas the Meckelin-CRD is formed by four helices and 11 β sheets (figs. S7 and S8B). Notably, the topology of the helix bundle of Meckelin-CRD is clearly distinct from that of class-F GPCRs-CRDs (fig. S10, A and B). In addition, the dimerization of the class-F GPCRs-CRDs displays a "helix-to-helix" packing fashion (*36*–*38*), whereas the Meckelin-CRDs form dimers with an antiparallel pattern (fig. S10, B and C). These results

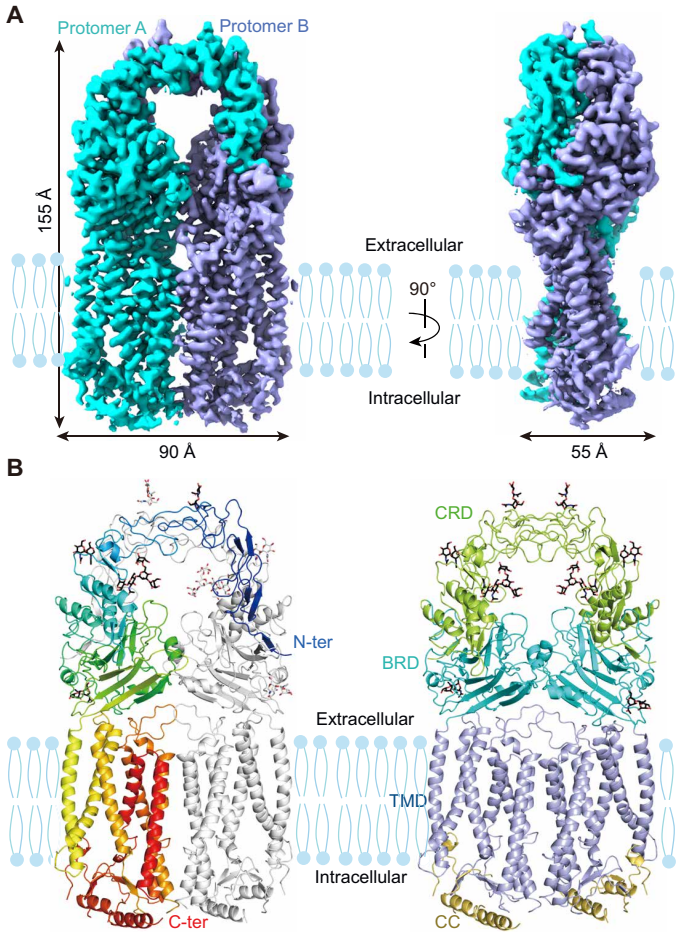

Fig. 1. Overall cryo-EM reconstruction of human Meckelin. (**A**) The overall EM density map of Meckelin. Meckelin is a homodimer, and protomers A and B are shown in cyan and light blue, respectively. The map was contoured at 0.018 and visualized in ChimeraX (*56*). (**B**) Overall structure of Meckelin. The structure on the left is colored in rainbow with the amino and carboxyl termini colored as blue and red, respectively. The structure on the right is domain colored. Meckelin contains a CRD, a BRD, a TMD, and a CC domain ter, terminus. The glycosyl groups are shown as black sticks. All structural figures were prepared in PyMOL (www.pymol.org).

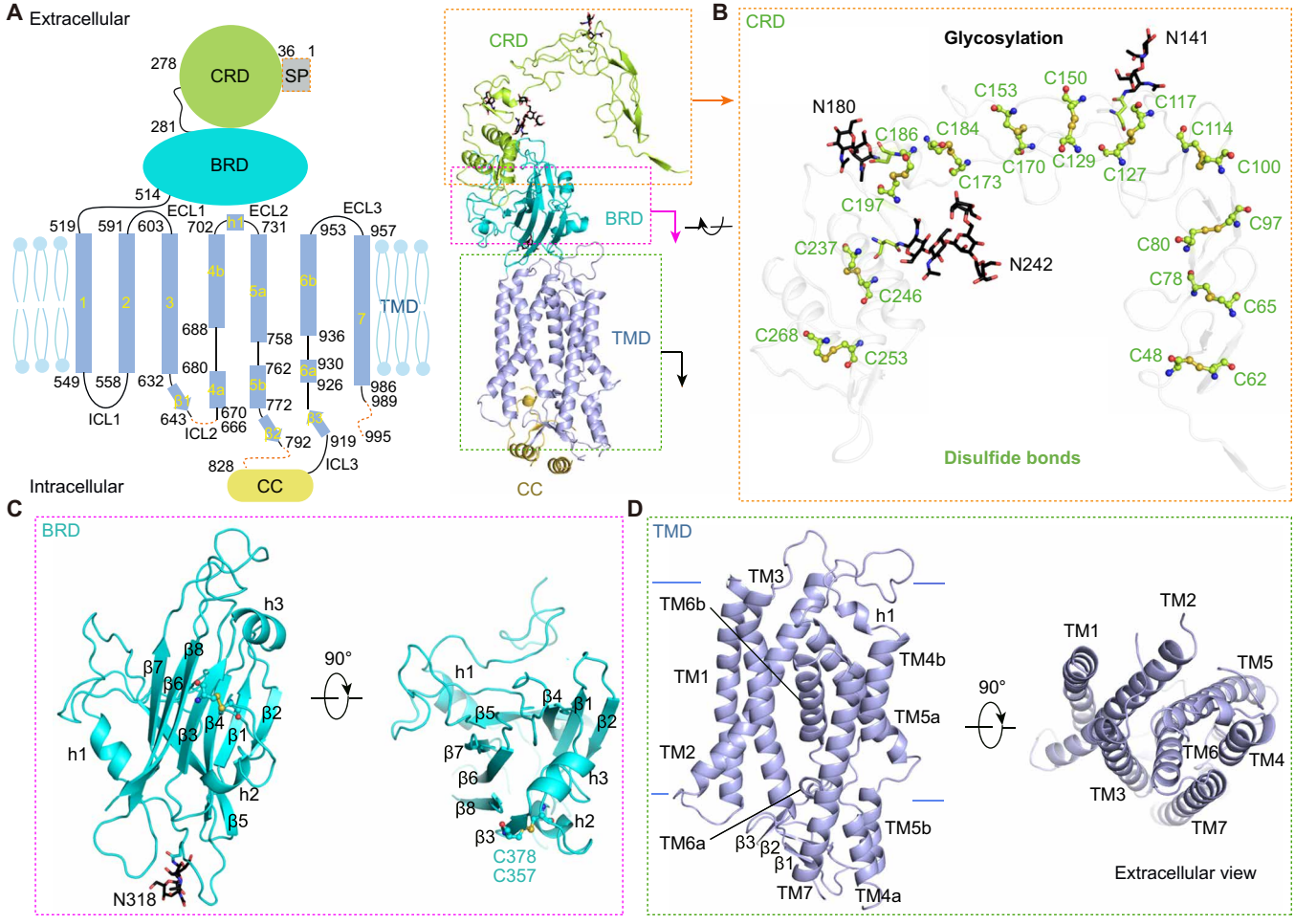

Fig. 2. The structural features of each domain. (**A**) Topological diagram and overall structure of one protomer. SP, signal peptide. Left: The orange dashed line indicates the invisible region in the structure, reflecting flexibility. (**B**) The CRD contains three glycosylation sites and 11 pairs of disulfide bonds, which maintain the stability and rigidity of CRD. (**C**) The BRD contains eight β sheets and three helices. In addition, one glycosylation site and one disulfide bond were observed. (**D**) The TMD contains seven transmembrane helices, wherein TM4 to TM6 were broken near the cytoplasmic surface of the membrane. The cytoplasmic portions of TM3, TM5, and TM6 are folded as β sheets. The cytoplasmic surface of TMD is sealed by these β sheets. TM6 is located in the middle of the helices bundle.

suggest that Meckelin-CRD is unique in structure and function. The electrostatic potential surface shows that a negatively charged region is located at the top of the Meckelin-CRD, surrounded by two positively charged regions (fig. S8C).

The structure of BRD

The BRD (residues 281 to 515) comprises three helices and eight β sheets (Fig. 2, A and C, and fig. S7). One disulfide bond and one glycosylation site were observed within the BRD (Fig. 2C). The BRD is the only extracellular structure that directly interacts with the TMD and thus may be responsible for signal transduction by allosteric coupling between conformational changes in the CRD and TMD (Fig. 2A and fig. S11A). The CRD/BRD interface is formed between the C terminus of CRD that contains an α-helical bundle (h2 to h4) and two β sheets (β10 and β11) and several loops of BRD that contain the N-terminal loop, the loop between β1 and β2, and the loop between β5 and β6 (Fig. 2C and fig. S11A). Extracellular loop 1 (ECL1) and ECL2 of the TMD mainly contribute to interactions with the BRD, wherein the contact surface is formed by the loop between h1 and β1, as well as the loop between β6 and β7, h2, β3, and β8 (Fig. 2C and fig. S11A).

The structure of TMD

Now, three TMD structures of FZDs have been determined, FZD_4, FZD_5, and FZD_7, suggesting intrinsic flexibility between the CRD and TMD (fig. S12B) (*36*–*38*). The SMO-CRD is perched on top of a small linker domain and directly contacts the TMD through an elongated transmembrane helix (fig. S12B) (*39*). In contrast, there was no direct interaction between the Meckelin-CRD and TMD, which were separated by a larger BRD (fig. S12A). For Meckelin-TMD, almost half of the helices (TM4 to TM6) are unwound near the intracellular surface of the membrane. The inclination of helices to the membrane varies substantially, wherein the angle between TM2 and TM5 reaches nearly 60°, and TM6a is almost perpendicular to the membrane (Fig. 2D). The cytoplasmic portions of TM3, TM5, and TM6 folds as β sheets (β1 to β3), forming a β sheet bundle with a β sheet of CC (Fig. 2A, right). This β sheet bundle structure seals the intracellular surface of the TMD (Fig. 2A, right). TM6 is

located at the center of the TMD, surrounded by TM2 to TM5 and TM7 (Fig. 2D). Although Meckelin also comprises a seven-transmembrane α-helical bundle structure, the topology is entirely different from that of class-F GPCRs, whose TMs are arranged counterclockwise (fig. S12).

Special structural elements, including the unwound portion of TM6, the TM6a perpendicular to the membrane, and the strong tilt of TM2 and TM5, form a pocket with a TM opening and an intracellular opening at the top and a narrow intracellular opening at the bottom (fig. S13, A and B). Numerous positively charged residues are present in the pocket (fig. S13B). Similarly, the structural elements, including the unwound portion of TM4 and TM5, form another positively charged pocket with a lateral intracellular opening (fig. S13C). In addition, a larger positively charged cavity with both a TM opening and an intracellular opening is formed within the TMD dimer because the pocket is located at the dimer interface (fig. S13, A and C).

Meckelin dimer interface

The dimer interface of Meckelin can be divided into four zones (Fig. 3A). The first zone is formed by the TM4s, TM5s, and TM7s of the TMDs (TMD-TMD′) through extensive hydrophobic interactions (Fig. 3B). At the extracellular end, TM4b interacts with TM4b′ and TM7′ of another protomer, forming a stable four-helix bundle (Fig. 3B). Near the cytoplasmic surface of the membrane, TM5a interacts with TM7′ (Fig. 3B). At the cytoplasmic end, TM4a interacts with TM4a′ and TM5b′ (Fig. 3B). The second zone is formed at the top of the CRDs (CRD-CRD′). In addition to some hydrophobic interactions, there are three hydrogen bonds and one cation-π contact (Fig. 3C).

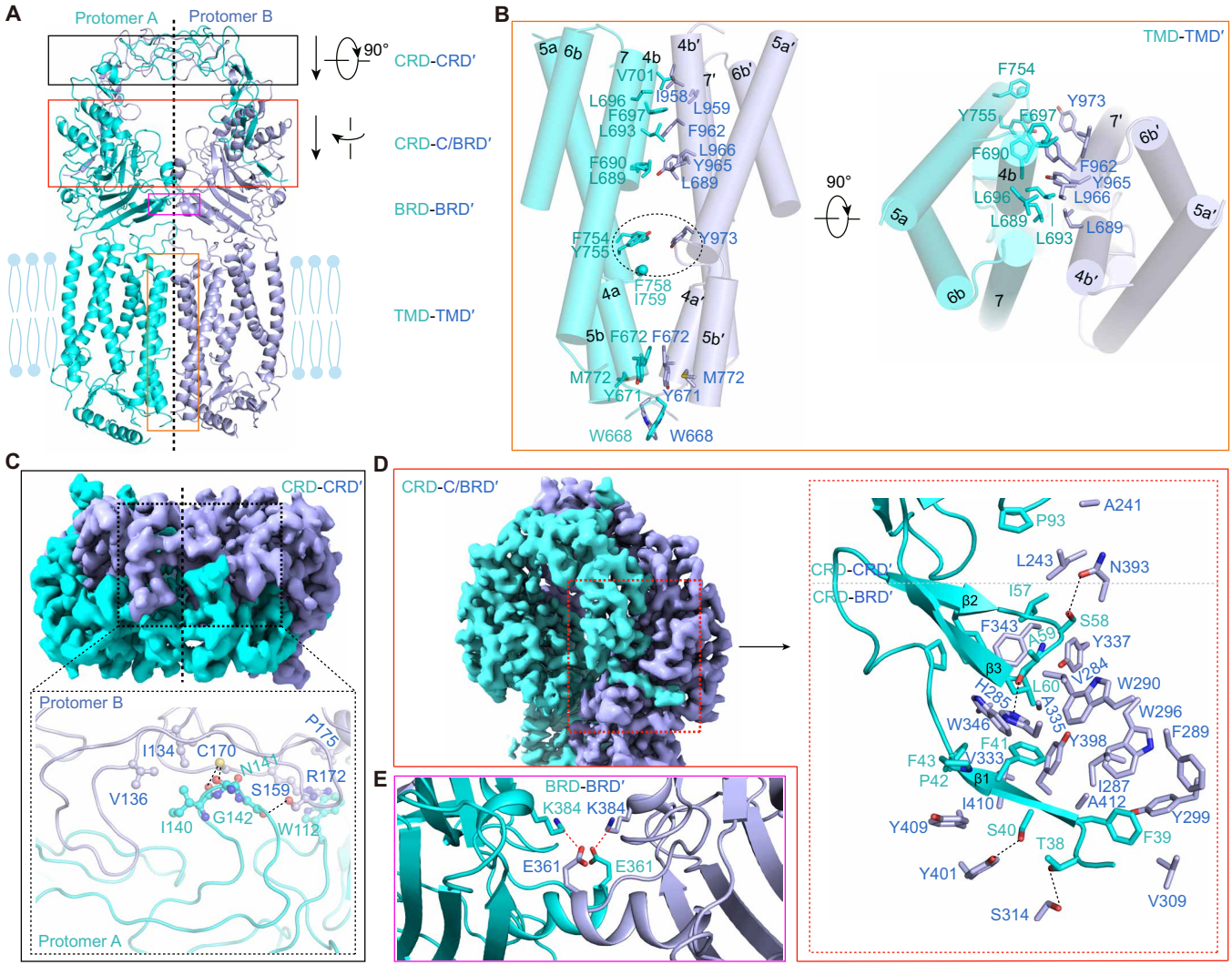

Fig. 3. Dimer interface of Meckelin. (**A**) The dimer interface of Meckelin can be divided into four zones. C/BRD′ indicates both CRD′ and BRD′ of the opposing protomer. (**B**) The zone of TMD-TMD′. TM4s, TM5s, and TM7s form the interface. The contact hydrophobic residues are indicated. (**C**) The zone of CRD-CRD′. In addition to hydrophobic interactions, a cation-π contact is formed between Arg^{172} and Trp^{112}, and hydrogen bonds are formed between Cys^{170} and Ile^{140}, Cys^{170} and Aln^{141}, as well as Gly^{142} and Ser^{159}. (**D**) The zone of CRD-C/BRD′. β1 of CRD reaches a hydrophobic pocket of BRD′ in the opposing protomer. In addition to extensive hydrophobic interactions, four hydrogen bonds are formed and are shown as dashed lines. (**E**) The zone of BRD-BRD′. An ionic interaction is formed between Lys^{384} of one protomer and Glu^{361} of the opposing protomer.

The third zone is mainly formed between the N terminus of the CRD of one protomer and BRD′ of another protomer, accompanied by minor interactions between the CRD and CRD′ (hereafter CRD-C/BRD′). The N terminus of the CRD is folded as a β sheet (β1), forming a β sheet bundle structure with β1, β2, β4, and β5 of the BRD′ of the opposing protomer. β1 of the CRD extends into a hydrophobic pocket of BRD′, mainly mediated by extensive hydrophobic interactions and two additional hydrogen bonds (Fig. 2D and fig. S11B). In addition, the loop between β2 and β3 of the CRD also interacts with the N-terminal loop of the BRD′. The loop between β6 and β7 of the CRD can interact with the loop between h2 and h3 of CRD′ by hydrophobic interactions (Fig. 2D and fig. S11B). The fourth zone is formed between the BRD and BRD′ by ionic interactions (Fig. 2E). Together, Meckelin forms a stable homodimer by extensive interactions through these four zones.

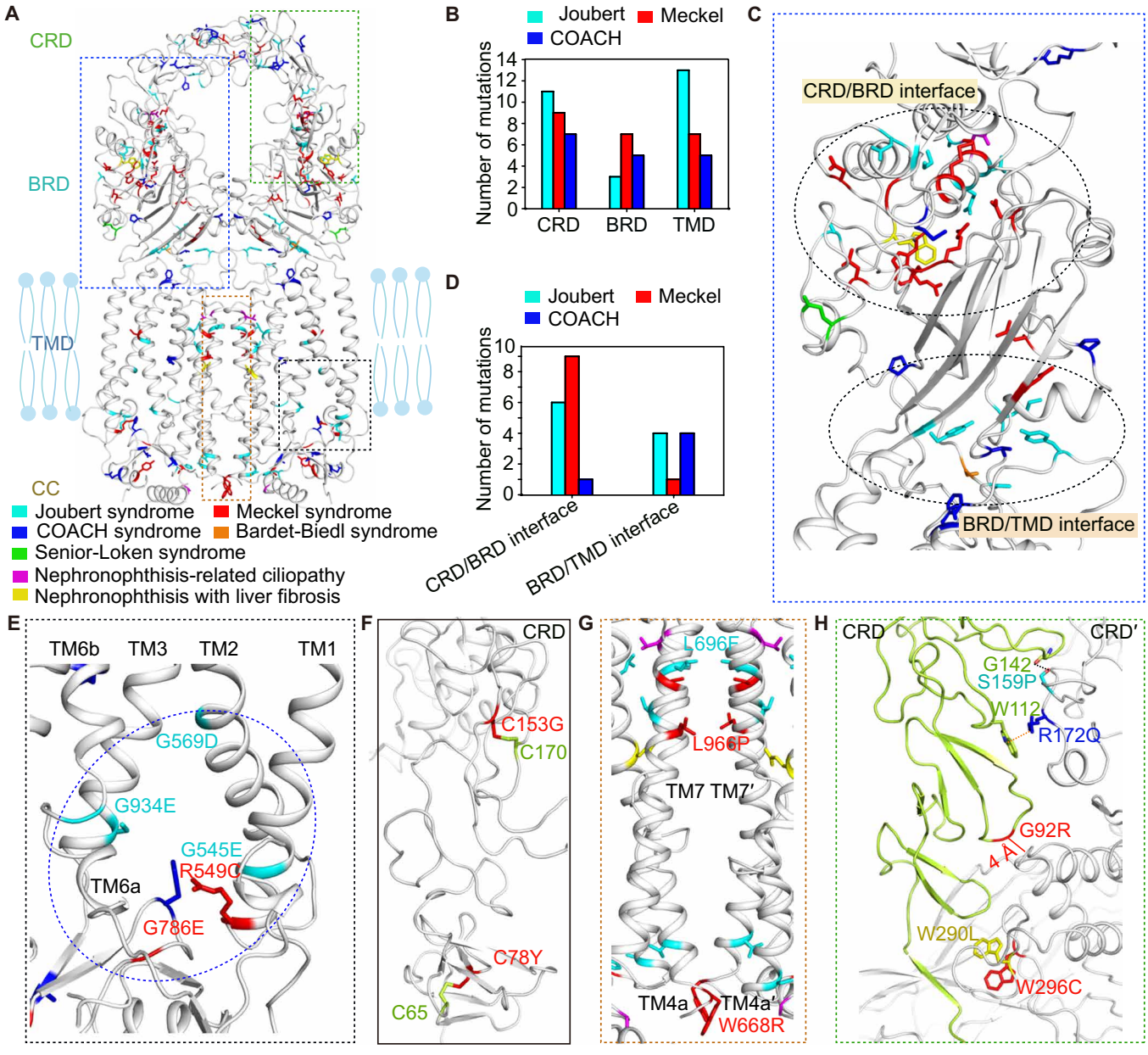

Fig. 4. Structural interpretation of the pathogenic mutations. (**A**) Structural mapping of the pathogenic mutations onto the structure of Meckelin. (**B**) Summary of the number of Joubert, Meckel, and COACH mutations in CRD, BRD, and TMD. (**C**) The CRD/BRD interface and BRD/TMD interface are two mutational hotspots, reflecting physiological importance. (**D**) Summary of the number of Joubert, Meckel, and COACH mutations at the domain interfaces. (**E**) The positively charged pocket formed by TM1 to TM3 and TM6 is a mutational hotspot. All of the mutations can affect the electrostatic property of this pocket, suggesting the functional importance of this pocket. (**F**) $Cys^{153}Gly$ and $Cys^{78}Trp$ may cause destabilization of the CRD by disturbing the formation of disulfide bonds. (**G** and **H**) Mutations located at the dimer interface are indicated. $Ser^{159}Pro$ disturbs the hydrogen bond between Ser^{159} and Gly^{142}. $Arg^{172}Gln$ disturbs the cation-π interaction between Arg^{172} and Trp^{112}. $Gly^{92}Arg$ may affect the dimer interaction by inducing steric hindrance.

Structural interpretation of the pathogenic mutations

In total, 81 missense mutations, most of which are associated with JBST, MKS, and COACH syndromes (Human Gene Mutations Database; www.hgmd.cf.ac.uk), have been identified in human Meckelin (table S2). Structural determination of Meckelin affords the opportunity to map a large number of disease mutations (Fig. 4A and table S2). Seventy-eight missense mutations could be reliably mapped to the structure, with 28 on the CRD, 18 on the BRD, 28 on the TMD, and 4 on the CC domain (Fig. 4, A and B). MKS- and COACH-derived mutations were almost evenly distributed in these three regions, whereas JBST-derived mutations in BRD were significantly less common than those in CRD and TMD (Fig. 4B).

Among the mapped disease mutations, the CRD/BRD interface and BRD/TMD interface harbor 17 and 9 residues, respectively, representing two hotspots and reflecting the physiological importance of the BRD in transducing signals from the CRD to the TMD (Fig. 4, C and D). These mutations may affect the conformational coupling of the functional domains. Notably, 10 of 24 MKS-derived mutations were mapped at the CRD/BRD interface (Fig. 4, C and D), suggesting that this region is particularly crucial for MKS. The large positively charged pocket formed by unwound TM6 harbors five mutations that all changed the charge (Fig. 4E), reflecting the functional importance of this structural element. The $Cys^{153}Gly$ and $Cys^{78}Tyr$ variants may cause destabilization of the arch bridge–like structure of CRD (Fig. 4F). Eight mutations are located at the dimer interface of Meckelin (Fig. 4, G and H), indicating that dimerization may be important for the function of Meckelin.

DISCUSSION

As cilia are found on almost all cells of the human body, most ciliopathies are syndromic rather than affecting only a single organ (*40*). Ciliopathies are characterized by the involvement of a core set of tissues—retinal, cerebral, and renal (*41*)—causing considerable dysfunction in affected patients. Although, overall, ciliopathies are considered rare diseases, they represent one of the fastest growing families of diseases (*40*). Meckelin, 1 of more than 180 established ciliopathy-associated proteins (*8*) represents an important drug target in the treatment of MKS, JBST, and COACH syndromes. Here, our structure offers a picture of the molecular appearance of human Meckelin.

Meckelin displays a previously unknown protein fold (Figs. 1 and 2). The unique folded pattern of Meckelin-CRD raises the question of how Meckelin recognizes the Wnt5a. A previous study showed that the missense mutations $Met^{252}Thr$, $Leu^{349}Ser$, $Gln^{376}Pro$, and $Arg^{440}Gln$ completely abolished the binding of Wnt5a to Meckelin (*12*), wherein $Met^{252}Thr$ and $Arg^{440}Gln$ are located at the CRD/BRD interface and $Leu^{349}Ser$ and $Gln^{376}Pro$ are located at the BRD/TMD interface, suggesting that these two domain interfaces identified as two mutational hotspots may play important roles in recognizing the Wnt5a. In this study, we confirmed that Wnt5a can interact with the intact Meckelin embedded in detergent micelles (fig. S14). The complex structure of Meckelin-Wnt5a remains to be determined to elucidate the underlying mechanisms for the recognition of Wnt5a by Meckelin.

Because of the breakage of TM4 to TM6 near the cytoplasmic surface of the membrane, two positively charged pockets with both a TM opening and an intracellular opening were formed (fig. S13). The structural features of the TM opening and intracellular opening were also observed in the structure of the adiponectin receptor, wherein a free fatty acid and a zinc molecule are located in a large internal cavity formed by the seven TMs, suggesting that the large opening is important for transferring molecules (*42*). These large openings in Meckelin may play a similar role in modulating the entry and exit of molecules into Meckelin, especially the negatively charged molecules. However, their precise roles need to be further investigated.

During the revision of our manuscript, the transformative artificial intelligence tool AlphaFold has predicted the structure of nearly the entire human proteome (*43*). Compared to the structure predicted by AlphaFold, our structure has a markedly different conformation (fig. S15), which may be caused by the combined effect of conformational change accompanying the dimerization and prediction errors.

The atomic structure of Meckelin provides a template for mapping a large number of disease mutations. However, elucidation of the functional mechanism of Meckelin and the disease mechanism of the dozens of mutations awaits further investigation. Our structure serves as a framework for future biochemical, biophysical, cellular, and computational analyses of Meckelin, facilitating drug development in treating its associated ciliopathies.

MATERIALS AND METHODS

Transient protein expression and purification

The full-length human *Meckelin* cDNA was obtained from the Han Jiahuai Lab, Xiamen University (Xiamen, Fujian, China) and subcloned into the pCAG vector with a C-terminal FLAG-tag and C-terminal His_6-tag. Human embryonic kidney (HEK) 293F cells (Invitrogen) were cultured in SMM 293T-II medium (Sino Biological Inc.) at 37°C under 5% CO_2 in a Multitron-Pro shaker (Infors; 130 rpm). When the cell density reached 2.0×10^6 cells/ml, the pCAG-*Meckelin* plasmids were transiently transfected into the cells. For 1-liter HEK293F cell culture, approximately 1.5 mg of plasmids was premixed with 4.0 mg of 25-kDa linear polyethylenimines (Polysciences) in 50 ml of fresh medium for 20 to 30 min before transfection. The 50 ml of mixture was then added to the cell culture. The transfected cells were cultured for 48 hours before harvesting.

For purification, 13 liters of cells was harvested by centrifugation at 800*g* for 10 min and resuspended in the lysis buffer containing 25 mM tris (pH 8.0), 150 mM NaCl, aprotinin (1.3 μg/ml), pepstatin (1 μg/ml), leupeptin (5 μg/ml), and 0.2 mM phenylmethylsulfonyl fluoride (lysis buffer A). The lysate was incubated in the buffer containing 2% (w/v) *n*-decyl-α-D-maltopyranoside (DM) (Anatrace) and 0.2% (w/v) cholesterol hemisuccinate (CHS) (Anatrace) at 4°C for 2 hours for membrane protein extraction. After ultracentrifugation at 18,700*g* for 40 min, the supernatant was collected and applied to the anti-FLAG M2 affinity gel (Sigma-Aldrich) at 4°C for two times. The resin was washed three times with 10 ml of wash buffer A (lysis buffer A plus 0.2% DM and 0.02% CHS). The protein was eluted with elution buffer A [wash buffer A plus FLAG peptide (200 μg/ml) (Sigma-Aldrich)]. The eluent was incubated with nickel affinity resin (Ni-NTA, Qiagen) at 4°C for 50 min, the resin was washed with wash buffer B [lysis buffer A plus 0.1% (w/v) digitonin (Sigma-Aldrich) and 10 mM imidazole], and the protein was eluted with elution buffer B (lysis buffer A plus 0.1% digitonin and 300 mM imidazole). The eluent was concentrated and subjected to size exclusion chromatography (Superose 6, 10/300, GE Healthcare) in a buffer containing 25 mM tris (pH 8.0), 150 mM NaCl, and 0.1%

digitonin. The peak fractions were pooled and concentrated to ~12 mg/ml for the cryo-EM analysis.

Cryo-EM data acquisition

Holey carbon grids (Quantifoil Au 300 mesh, R1.2/1.3) were glow-discharged in the Plasma Cleaner PDC-32G-2 (Harrick Plasma Company) with a vacuum for 2 min and mid force for 30 s. Aliquots (3 μl) of Meckelin protein were placed on the glow-discharged grids, which were then blotted for 3 s and flash-frozen in liquid ethane cooled by liquid nitrogen using Vitrobot Mark IV (Thermo Fisher Scientific) at 8°C and 100% humidity. The grids were loaded onto a 300-kV Titan Krios (Thermo Fisher Scientific Inc.) equipped with a K3 Summit detector (Gatan) and a GIF Quantum energy filter. Images were automatically collected using AutoEMation (*44*) in super-resolution mode at a nominal magnification of ×81,000, with a slit width of 20 eV on the energy filter. A defocus series ranging from −1.2 to −2.2 μm was used. Each stack was exposed for 2.56 s with an exposure time of 0.08 s per frame, resulting in a total of 32 frames per stack, and the total dose was approximately 50 $e^{-}/Å^{2}$ for each stack. The stacks were motion-corrected with MotionCor2 (*45*) and binned twofold, resulting in a pixel size of 1.087 Å per pixel. Meanwhile, dose weighting was performed (*46*). The defocus values were estimated with Gctf (*47*).

Image processing

A diagram for the data processing is presented in fig. S2. A total of 5219 micrographs were collected, and particles were automatically picked with Gautomatch (developed by K. Zhang; www2.mrc-lmb.cam.ac.uk/research/locally-developed-software/zhang-software/#gauto). After 2D classification with RELION and cryoSPARC (*48*–*51*), the particles from good classes were used to generate an initial model with one class and C1 symmetry using RELION. A total of 1,025,507 good particles were subjected to global angular search three-dimensional (3D) classification with one class and C1 symmetry. Then, the particles were further subjected to 3D classification with 10 classes and a local angular search step of 3.75°. The local angular search 3D classification was performed several times, with the output from different iterations of the global angular search 3D classification as input. The selected good particles were subjected to local angular search 3D autorefinement, resulting in a 4.3-Å resolution map. Three cycles of multireference 3D classification with four classes were performed to further remove bad particles. The references include the 4.3-Å resolution map and three low-pass–filtered maps (6, 8, and 10 Å). The 219,967 selected good particles were subjected to the final 3D autorefinement without imposing symmetry, resulting in 3D maps with an overall resolution of 3.4 Å. The final resolution was increased to 3.3 Å when applied to C2 symmetry. To trace the main chain of the CC domain, the particles were further applied for symmetry expansion using relion_particle_symmetry_expand in RELION. The resolution was estimated with the gold-standard Fourier shell correlation 0.143 criterion (*52*) with high-resolution noise substitution (*53*).

Model building and structure refinement

The 3.3-Å EM map was used for de novo model building of the overall structure of Meckelin due to the lack of an available homolog structure. For the TMD, a ploy-Ala model was first built manually in Coot (*54*). Sequence assignment was guided mainly by bulky residues such as Phe, Tyr, Trp, and Arg. Unique patterns of sequences were exploited for validation of residue assignment. For the ECD (CRD and BRD), four glycosylation sites with obvious sugar densities and 12 pairs of disulfide bonds in the ECD also facilitated sequence assignment. For the CC domain, sequence assignment was guided mainly by bulky residues resolved in the EM map with symmetry expansion. Structure refinements were carried out by Phenix in real space with secondary structure and geometry restraints (*55*). The statistics of the 3D reconstruction and model refinement are summarized in table S1.

In vitro pull-down assays

The full-length cDNAs for human *Meckelin*, *Wnt5a*, and rice *HKT2.2* were subcloned into the pCAG vector with a C-terminal FLAG-tag, a C-terminal Strep-tag, and a N-terminal FLAG-tag, respectively. HKT2.2, a sodium and potassium transporter, serves as a negative control. The pCAG-*Meckelin*-FLAG plus pCAG-*Wnt5a*-Strep plasmids, the pCAG-FLAG-*HKT2.2* plus pCAG-*Wnt5a*-Strep plasmids, and the pCAG-*Meckelin*-FLAG plasmids were transiently transfected into HEK293F cells, respectively. Cells were collected and resuspended in the lysis buffer A plus 2% (w/v) *n*-dodecyl-α-D-maltopyranoside (DDM; Anatrace) and 0.2% (w/v) CHS 48 hours after transfection. After incubation at 4°C for 2 hours, the mixture was applied to centrifugation at 24,000*g* at 4°C for 40 min, and equal amount of the supernatant was applied to the anti-FLAG M2 affinity gel (Sigma-Aldrich) and Strep-Tactin Sepharose (IBA Lifesciences), respectively. The resin was rinsed four times with the wash buffer C (lysis buffer A plus 0.02% DDM and 0.002% CHS). The proteins were eluted with elution buffer C [wash buffer C plus FLAG peptide (200 μg/ml)] and elution buffer D [wash buffer C plus 2.5 mM D-desthiobiotin (IBA Lifesciences)] and analyzed by Western blot.

For Western blotting, the proteins were transferred to Immobilon-P transfer membranes (Millipore) after SDS–polyacrylamide gel electrophoresis. The membranes were blocked by 5% (w/v) nonfat powdered milk (BBI) at room temperature for 1 hour and incubated with the primary antibodies [anti–FLAG-tag mouse monoclonal antibody (Cwbio) for Meckelin and HKT2.2 or anti–Strep-tag mouse monoclonal antibody (Easybio) for Wnt5a] at room temperature for 1 hour with a 1:3000 dilution. Then, the membranes were washed four times with the TBST (Tris Buffered Saline with Tween 20) buffer that contained 25 mM tris (pH 8.0), 150 mM NaCl, and 0.05% (w/v) Tween 20. The bound antibodies were visualized by chemiluminescence (Super ECL Detection Reagent, Yeasen) using a 1:10,000 dilution of goat anti-mouse immunoglobulin G antibody, horseradish peroxidase conjugates, as the secondary antibody (CWBIO). Membranes were exposed by Amersham Imager 680 (GE Healthcare).

SUPPLEMENTARY MATERIALS

Supplementary material for this article is available at https://science.org/doi/10.1126/sciadv.abj9748

View/request a protocol for this paper from *Bio-protocol*.

REFERENCES AND NOTES

1. M. Fliegauf, T. Benzing, H. Omran, When cilia go bad: Cilia defects and ciliopathies. *Nat. Rev. Mol. Cell Biol.* **8**, 880–893 (2007).
2. H. A. Praetorius, K. R. Spring, Bending the MDCK cell primary cilium increases intracellular calcium. *J. Membr. Biol.* **184**, 71–79 (2001).
3. S. M. Nauli, F. J. Alenghat, Y. Luo, E. Williams, P. Vassilev, X. Li, A. E. H. Elia, W. Lu, E. M. Brown, S. J. Quinn, D. E. Ingber, J. Zhou, Polycystins 1 and 2 mediate mechanosensation in the primary cilium of kidney cells. *Nat. Genet.* **33**, 129–137 (2003).

4. D. Huangfu, A. Liu, A. S. Rakeman, N. S. Murcia, L. Niswander, K. V. Anderson, Hedgehog signalling in the mouse requires intraflagellar transport proteins. *Nature* **426**, 83–87 (2003).
5. M. Simons, J. Gloy, A. Ganner, A. Bullerkotte, M. Bashkurov, C. Krönig, B. Schermer, T. Benzing, O. A. Cabello, A. Jenny, M. Mlodzik, B. Polok, W. Driever, T. Obara, G. Walz, Inversin, the gene product mutated in nephronophthisis type II, functions as a molecular switch between Wnt signaling pathways. *Nat. Genet.* **37**, 537–543 (2005).
6. L. Schneider, C. A. Clement, S. C. Teilmann, G. J. Pazour, E. K. Hoffmann, P. Satir, S. T. Christensen, PDGFRαα signaling is regulated through the primary cilium in fibroblasts. *Curr. Biol.* **15**, 1861–1866 (2005).
7. S. Nonaka, Y. Tanaka, Y. Okada, S. Takeda, A. Harada, Y. Kanai, M. Kido, N. Hirokawa, Randomization of left-right asymmetry due to loss of nodal cilia generating leftward flow of extraembryonic fluid in mice lacking KIF3B motor protein. *Cell* **95**, 829–837 (1998).
8. D. J. McConnachie, J. L. Stow, A. J. Mallett, Ciliopathies and the kidney: A review. *Am. J. Kidney Dis.* **77**, 410–419 (2021).
9. H. Ishikawa, W. F. Marshall, Ciliogenesis: Building the cell's antenna. *Nat. Rev. Mol. Cell Biol.* **12**, 222–234 (2011).
10. F. R. Garcia-Gonzalo, K. C. Corbit, M. S. Sirerol-Piquer, G. Ramaswami, E. A. Otto, T. R. Noriega, A. D. Seol, J. F. Robinson, C. L. Bennett, D. J. Josifova, J. M. García-Verdugo, N. Katsanis, F. Hildebrandt, J. F. Reiter, A transition zone complex regulates mammalian ciliogenesis and ciliary membrane composition. *Nat. Genet.* **43**, 776–784 (2011).
11. L. Sang, J. J. Miller, K. C. Corbit, R. H. Giles, M. J. Brauer, E. A. Otto, L. M. Baye, X. Wen, S. J. Scales, M. Kwong, E. G. Huntzicker, M. K. Sfakianos, W. Sandoval, J. F. Bazan, P. Kulkarni, F. R. Garcia-Gonzalo, A. D. Seol, J. F. O'Toole, S. Held, H. M. Reutter, W. S. Lane, M. A. Rafiq, A. Noor, M. Ansar, A. R. R. Devi, V. C. Sheffield, D. C. Slusarski, J. B. Vincent, D. A. Doherty, F. Hildebrandt, J. F. Reiter, P. K. Jackson, Mapping the NPHP-JBTS-MKS protein network reveals ciliopathy disease genes and pathways. *Cell* **145**, 513–528 (2011).
12. Z. A. Abdelhamed, S. Natarajan, G. Wheway, C. F. Inglehearn, C. Toomes, C. A. Johnson, D. J. Jagger, The Meckel-Gruber syndrome protein TMEM67 controls basal body positioning and epithelial branching morphogenesis in mice via the non-canonical Wnt pathway. *Dis. Model. Mech.* **8**, 527–541 (2015).
13. V. Hartill, K. Szymanska, S. M. Sharif, G. Wheway, C. A. Johnson, Meckel-Gruber syndrome: An update on diagnosis, clinical management, and research advances. *Front. Pediatr.* **5**, 244 (2017).
14. C. Sergi, S. Adam, P. Kahl, H. F. Otto, Study of the malformation of ductal plate of the liver in Meckel syndrome and review of other syndromes presenting with this anomaly. *Pediatr. Dev. Pathol.* **3**, 568–583 (2000).
15. I. D. Young, A. B. Rickett, M. Clarke, High incidence of Meckel's syndrome in Gujarati Indians. *J. Med. Genet.* **22**, 301–304 (1985).
16. H. N. Al Yaqoubi, N. Fatema, Meckel Gruber syndrome associated with anencephaly—An unusual reported case. *Oxf. Med. Case Reports* **2018**, omx092 (2018).
17. M. Iannicelli, F. Brancati, S. Mougou-Zerelli, A. Mazzotta, S. Thomas, N. Elkhartoufi, L. Travaglini, C. Gomes, G. L. Ardissino, E. Bertini, E. Boltshauser, P. Castorina, S. D'Arrigo, R. Fischetto, B. Leroy, P. Loget, M. Bonnière, L. Starck, J. Tantau, B. Gentilin, S. Majore, D. Swistun, E. Flori, F. Lalatta, C. Pantaleoni, J. Penzien, P. Grammatico; International JSRD Study Group, B. Dallapiccola, J. G. Gleeson, T. Attie-Bitach, E. M. Valente, Novel TMEM67 mutations and genotype-phenotype correlates in meckelin-related ciliopathies. *Hum. Mutat.* **31**, E1319–E1331 (2010).
18. F. Brancati, M. Iannicelli, L. Travaglini, A. Mazzotta, E. Bertini, E. Boltshauser, S. D'Arrigo, F. Emma, E. Fazzi, R. Gallizzi, M. Gentile, D. Loncarevic, V. Mejaski-Bosnjak, C. Pantaleoni, L. Rigoli, C. D. Salpietro, S. Signorini, G. R. Stringini, A. Verloes, D. Zabloka; the International JSRD Study Group, B. Dallapiccola, J. G. Gleeson, E. M. Valente, *MKS3/TMEM67* mutations are a major cause of COACH syndrome, a Joubert Syndrome related disorder with liver involvement. *Hum. Mutat.* **30**, E432–E442 (2009).
19. Z. A. Abdelhamed, G. Wheway, K. Szymanska, S. Natarajan, C. Toomes, C. Inglehearn, C. A. Johnson, Variable expressivity of ciliopathy neurological phenotypes that encompass Meckel-Gruber syndrome and Joubert syndrome is caused by complex de-regulated ciliogenesis, Shh and Wnt signalling defects. *Hum. Mol. Genet.* **22**, 1358–1372 (2013).
20. V. Cantagrel, J. L. Silhavy, S. L. Bielas, D. Swistun, S. E. Marsh, J. Y. Bertrand, S. Audollent, T. Attié-Bitach, K. R. Holden, W. B. Dobyns, D. Traver, L. Al-Gazali, B. R. Ali, T. H. Lindner, T. Caspary, E. A. Otto, F. Hildebrandt, I. A. Glass, C. V. Logan, C. A. Johnson, C. Bennett, F. Brancati; International Joubert Syndrome Related Disorders Study Group, E. M. Valente, C. G. Woods, J. G. Gleeson, Mutations in the cilia gene *ARL13B* lead to the classical form of Joubert syndrome. *Am. J. Hum. Genet.* **83**, 170–179 (2008).
21. M. D. Weiland, M. J. Nowicki, J. K. Jones, H. W. Giles, COACH syndrome: An unusual cause of neonatal cholestasis. *J. Pediatr.* **158**, 858–858.e1 (2011).
22. U. M. Smith, M. Consugar, L. J. Tee, B. M. McKee, E. N. Maina, S. Whelan, N. V. Morgan, E. Goranson, P. Gissen, S. Lilliquist, I. A. Aligianis, C. J. Ward, S. Pasha, R. Punyashthiti, S. Malik Sharif, P. A. Batman, C. P. Bennett, C. G. Woods, C. McKeown, M. Bucourt, C. A. Miller, P. Cox, L. AlGazali, R. C. Trembath, V. E. Torres, T. Attie-Bitach, D. A. Kelly, E. R. Maher, V. H. Gattone II, P. C. Harris, C. A. Johnson, The transmembrane protein meckelin (MKS3) is mutated in Meckel-Gruber syndrome and the wpk rat. *Nat. Genet.* **38**, 191–196 (2006).
23. R. Nusse, H. Clevers, Wnt/β-catenin signaling, disease, and emerging therapeutic modalities. *Cell* **169**, 985–999 (2017).
24. C. L. Williams, C. Li, K. Kida, P. N. Inglis, S. Mohan, L. Semenec, N. J. Bialas, R. M. Stupay, N. Chen, O. E. Blacque, B. K. Yoder, M. R. Leroux, MKS and NPHP modules cooperate to establish basal body/transition zone membrane associations and ciliary gate function during ciliogenesis. *J. Cell Biol.* **192**, 1023–1041 (2011).
25. M. Adams, R. J. Simms, Z. Abdelhamed, H. R. Dawe, K. Szymanska, C. V. Logan, G. Wheway, E. Pitt, K. Gull, M. A. Knowles, E. Blair, S. H. Cross, J. A. Sayer, C. A. Johnson, A meckelin–filamin A interaction mediates ciliogenesis. *Hum. Mol. Genet.* **21**, 1272–1286 (2012).
26. H. R. Dawe, U. M. Smith, A. R. Cullinane, D. Gerrelli, P. Cox, J. L. Badano, S. Blair-Reid, N. Sriram, N. Katsanis, T. Attie-Bitach, S. C. Afford, A. J. Copp, D. A. Kelly, K. Gull, C. A. Johnson, The Meckel-Gruber Syndrome proteins MKS1 and meckelin interact and are required for primary cilium formation. *Hum. Mol. Genet.* **16**, 173–186 (2007).
27. T. J. Park, S. L. Haigo, J. B. Wallingford, Ciliogenesis defects in embryos lacking inturned or fuzzy function are associated with failure of planar cell polarity and Hedgehog signaling. *Nat. Genet.* **38**, 303–311 (2006).
28. C. Jones, V. C. Roper, I. Foucher, D. Qian, B. Banizs, C. Petit, B. K. Yoder, P. Chen, Ciliary proteins link basal body polarization to planar cell polarity regulation. *Nat. Genet.* **40**, 69–77 (2008).
29. H. R. Dawe, M. Adams, G. Wheway, K. Szymanska, C. V. Logan, A. A. Noegel, K. Gull, C. A. Johnson, Nesprin-2 interacts with meckelin and mediates ciliogenesis via remodelling of the actin cytoskeleton. *J. Cell Sci.* **122**, 2716–2726 (2009).
30. Z. A. Abdelhamed, D. I. Abdelmottaleb, M. E. el-Asrag, S. Natarajan, G. Wheway, C. F. Inglehearn, C. Toomes, C. A. Johnson, The ciliary Frizzled-like receptor Tmem67 regulates canonical Wnt/β-catenin signalling in the developing cerebellum via Hoxb5. *Sci. Rep.* **9**, 5446 (2019).
31. E. Du, H. Li, S. Jin, X. Hu, M. Qiu, R. Han, Evidence that TMEM67 causes polycystic kidney disease through activation of JNK/ERK-dependent pathways. *Cell Biol. Int.* **37**, 694–702 (2013).
32. J. N. Anastas, R. T. Moon, WNT signalling pathways as therapeutic targets in cancer. *Nat. Rev. Cancer* **13**, 11–26 (2013).
33. J. Briscoe, P. P. Therond, The mechanisms of Hedgehog signalling and its roles in development and disease. *Nat. Rev. Mol. Cell Biol.* **14**, 416–429 (2013).
34. Y. K. Xu, R. Nusse, The Frizzled CRD domain is conserved in diverse proteins including several receptor tyrosine kinases. *Curr. Biol.* **8**, R405–R406 (1998).
35. X. Zhang, S. Dong, F. Xu, Structural and druggability landscape of frizzled G protein-coupled receptors. *Trends Biochem. Sci.* **43**, 1033–1046 (2018).
36. N. Tsutsumi, S. Mukherjee, D. Waghray, C. Y. Janda, K. M. Jude, Y. Miao, J. S. Burg, N. G. Aduri, A. A. Kossiakoff, C. Gati, K. C. Garcia, Structure of human Frizzled5 by fiducial-assisted cryo-EM supports a heterodimeric mechanism of canonical Wnt signaling. *eLife* **9**, e58464 (2020).
37. S. Yang, Y. Wu, T.-H. Xu, P. W. de Waal, Y. He, M. Pu, Y. Chen, Z. J. DeBruine, B. Zhang, S. A. Zaidi, P. Popov, Y. Guo, G. W. Han, Y. Lu, K. Suino-Powell, S. Dong, K. G. Harikumar, L. J. Miller, V. Katritch, H. E. Xu, W. Shui, R. C. Stevens, K. Melcher, S. Zhao, F. Xu, Crystal structure of the Frizzled 4 receptor in a ligand-free state. *Nature* **560**, 666–670 (2018).
38. L. Xu, B. Chen, H. Schihada, S. C. Wright, A. Turku, Y. Wu, G. W. Han, M. Kowalski-Jahn, P. Kozielewicz, C. F. Bowin, X. Zhang, C. Li, M. Bouvier, G. Schulte, F. Xu, Cryo-EM structure of constitutively active human Frizzled 7 in complex with heterotrimeric G_s. *Cell Res.* 10.1038/s41422-021-00525-6 (2021).
39. E. F. X. Byrne, R. Sircar, P. S. Miller, G. Hedger, G. Luchetti, S. Nachtergaele, M. D. Tully, L. Mydock-McGrane, D. F. Covey, R. P. Rambo, M. S. P. Sansom, S. Newstead, R. Rohatgi, C. Siebold, Structural basis of Smoothened regulation by its extracellular domains. *Nature* **535**, 517–522 (2016).
40. M. Duong Phu, S. Bross, M. D. Burkhalter, M. Philipp, Limitations and opportunities in the pharmacotherapy of ciliopathies. *Pharmacol. Ther.* **225**, 107841 (2021).
41. J. F. Reiter, M. R. Leroux, Genes and molecular pathways underpinning ciliopathies. *Nat. Rev. Mol. Cell Biol.* **18**, 533–547 (2017).
42. I. Vasiliauskaite-Brooks, R. Sounier, P. Rochaix, G. Bellot, M. Fortier, F. Hoh, L. De Colibus, C. Bechara, E. M. Saied, C. Arenz, C. Leyrat, S. Granier, Structural insights into adiponectin receptors suggest ceramidase activity. *Nature* **544**, 120–123 (2017).
43. J. Jumper, R. Evans, A. Pritzel, T. Green, M. Figurnov, O. Ronneberger, K. Tunyasuvunakool, R. Bates, A. Žídek, A. Potapenko, A. Bridgland, C. Meyer, S. A. A. Kohl, A. J. Ballard, A. Cowie, B. Romera-Paredes, S. Nikolov, R. Jain, J. Adler, T. Back, S. Petersen, D. Reiman, E. Clancy, M. Zielinski, M. Steinegger, M. Pacholska, T. Berghammer, S. Bodenstein, D. Silver, O. Vinyals, A. W. Senior, K. Kavukcuoglu, P. Kohli, D. Hassabis, Highly accurate protein structure prediction with AlphaFold. *Nature* **596**, 590–596 (2021).

44. J. Lei, J. Frank, Automated acquisition of cryo-electron micrographs for single particle reconstruction on an FEI Tecnai electron microscope. *J. Struct. Biol.* **150**, 69–80 (2005).
45. S. Q. Zheng, E. Palovcak, J.-P. Armache, K. A. Verba, Y. Cheng, D. A. Agard, MotionCor2: Anisotropic correction of beam-induced motion for improved cryo-electron microscopy. *Nat. Methods* **14**, 331–332 (2017).
46. T. Grant, N. Grigorieff, Measuring the optimal exposure for single particle cryo-EM using a 2.6 Å reconstruction of rotavirus VP6. *eLife* **4**, e06980 (2015).
47. K. Zhang, Gctf: Real-time CTF determination and correction. *J. Struct. Biol.* **193**, 1–12 (2016).
48. D. Kimanius, B. O. Forsberg, S. H. Scheres, E. Lindahl, Accelerated cryo-EM structure determination with parallelisation using GPUs in RELION-2. *eLife* **5**, e18722 (2016).
49. S. H. W. Scheres, RELION: Implementation of a Bayesian approach to cryo-EM structure determination. *J. Struct. Biol.* **180**, 519–530 (2012).
50. S. H. W. Scheres, Semi-automated selection of cryo-EM particles in RELION-1.3. *J. Struct. Biol.* **189**, 114–122 (2015).
51. A. Punjani, J. L. Rubinstein, D. J. Fleet, M. A. Brubaker, cryoSPARC: Algorithms for rapid unsupervised cryo-EM structure determination. *Nat. Methods* **14**, 290–296 (2017).
52. P. B. Rosenthal, R. Henderson, Optimal determination of particle orientation, absolute hand, and contrast loss in single-particle electron cryomicroscopy. *J. Mol. Biol.* **333**, 721–745 (2003).
53. S. Chen, G. McMullan, A. R. Faruqi, G. N. Murshudov, J. M. Short, S. H. W. Scheres, R. Henderson, High-resolution noise substitution to measure overfitting and validate resolution in 3D structure determination by single particle electron cryomicroscopy. *Ultramicroscopy* **135**, 24–35 (2013).
54. P. Emsley, B. Lohkamp, W. G. Scott, K. Cowtan, Features and development of Coot. *Acta Crystallogr. D Biol. Crystallogr.* **66**, 486–501 (2010).
55. P. D. Adams, P. V. Afonine, G. Bunkóczi, V. B. Chen, I. W. Davis, N. Echols, J. J. Headd, L.-W. Hung, G. J. Kapral, R. W. Grosse-Kunstleve, A. J. McCoy, N. W. Moriarty, R. Oeffner, R. J. Read, D. C. Richardson, J. S. Richardson, T. C. Terwilliger, P. H. Zwart, PHENIX: A comprehensive Python-based system for macromolecular structure solution. *Acta Crystallogr. D Biol. Crystallogr.* **66**, 213–221 (2010).
56. T. D. Goddard, C. C. Huang, E. C. Meng, E. F. Pettersen, G. S. Couch, J. H. Morris, T. E. Ferrin, UCSF ChimeraX: Meeting modern challenges in visualization and analysis. *Protein Sci.* **27**, 14–25 (2018).

Acknowledgments: We thank the Cryo-EM Facility and Supercomputer Center of Westlake University for providing data collection and computation support, respectively. **Funding:** D.G. is supported by funding from the Nankai University. **Author contributions:** D.G. conceived the project. D.L. and D.Q. performed the experiments. H.S solved the structure, and D.G. built the atomic model. All authors contributed to the data analysis. D.G. wrote the manuscript. **Competing interests:** The authors declare that they have no competing interests. **Data and materials availability:** All data needed to evaluate the conclusions in the paper are present in the paper and/or the Supplementary Materials. The atomic coordinate (PDB: 7FH1) and EM density map (EMDB: EMD-31584) of Meckelin have been deposited in the Protein Data Bank (www.rcsb.org) and the Electron Microscopy Data Bank (www.ebi.ac.uk/pdbe/emdb/).

Submitted 14 June 2021
Accepted 15 September 2021
Published 3 November 2021
10.1126/sciadv.abj9748